Earth and Planetary Science Letters, 71 (1984) 263–278
Elsevier Science Publishers B.V., Amsterdam – Printed in The Netherlands

[4]

Electron probe microanalysis study on processes of low-temperature oxidation of titanomagnetite

Takatoshi Akimoto [1,*], Hajimu Kinoshita [1] and Toshio Furuta [2]

[1] *Department of Earth Sciences, Chiba University, Chiba 260 (Japan)*
[2] *Ocean Research Institute, University of Tokyo, Nakano, Tokyo 164 (Japan)*

Received February 15, 1984
Revised version received August 30, 1984

Partially oxidized titanomagnetite grains in various kinds of volcanic rocks were investigated by electron probe microanalyzer (EPMA) in order to clarify the process of oxidation at low temperature. The following results were obtained by the present investigation: (1) Primary composition of titanomagnetite is homogeneous in individual grains, although variation in composition among different grains is observed on each thin section. (2) Migration of Fe cations during low-temperature oxidation is clearly seen in all oxidized grains. Some other constituent cations are also bleached and consequently the relative content of the remaining cations becomes large. (3) The detailed internal structures of titanomagnetite grains are observed as backscattered electron images (BEI) with an electronprobe microanalyzer, and it seems likely that the structures depend upon the degree of low-temperature oxidation. (4) The chemical and physical properties of oxidized titanomagnetites imply that low-temperature oxidation is not a simple process but a complex one. Such an oxidation process is correlatable to both the mobility of cation and the oxidation condition such as a circulation of some active hydrothermal materials at low temperature.

1. Introduction

Alteration of magnetic minerals contained in igneous rocks has been studied by many authors using mainly submarine basalts [1–3]. These studies suggest that the crustal rocks have been altered to some extent by cold water. Trends of decay of the marine magnetic anomaly patterns with increasing distance from the oceanic ridge axes are attributed to the submarine weathering of titanomagnetites with increasing age of the oceanic crust [4]. The weathering (or alteration) of titanomagnetites is generally called low-temperature oxidation in contrast to high-temperature oxidation at temperatures considerably higher than 600°C. Low-temperature oxidation has been described as a simple oxidation process without any changes in the cation content in the titanomagnetite crystal [5–9]. However, recent studies have shown that low-temperature oxidation in nature occurs as complex processes [2,3,10]. The occurrence and degree of alteration of titanomagnetites provide a great deal of information on the process of low-temperature oxidation. During the last two decades, studies on low-temperature oxidation have clarified the mechanism of oxidation [11], its effect on the primary remanence intensities [1,12] and chemical processes [3,13]. However, quantitative descriptions of the chemical change and cation deficiency in titanomagnetite induced by low-temperature oxidation are not sufficient to explain these phenomena occurring in nature. This is mainly because titanomagnetite grains in submarine pillow basalts have dimensions too small to be analyzed by microscope and electron probe microanalyzer. Low-temperature oxidation can be observed in submarine basalts in different places of the world regardless of their ages. Earlier studies on oxide minerals of submarine basalts showed that the contents of Fe and Ti cations in primary

* Present address: Makuhari-kita Highschool, Wakaba, Chiba 281, Japan.

0012-821X/84/$03.00

unoxidized titanomagnetite seem to be homogeneous with a Ti/Fe ratio of about 0.25 [2,10]. However, recent studies demonstrated that the primary Fe and Ti contents in some basalts are considerably scattered and that the Ti/Fe ratio varies from 0.1 to 0.3 [14,15].

The degree of oxidation of each sample [5] can be correlated with properties such as Curie temperature, lattice parameter and bulk chemical composition of the whole sample. However, each grain may be oxidized to a different degree. The degree of oxidation in a relatively large grain (larger than 10 μm titanomagnetite) may also be different from part to part when the grain is partially oxidized. From this viewpoint it is clear that the degree of oxidation of the whole sample is only an averaged chemical property of the titanomagnetite grains with large chemical heterogeneity.

One objective of this paper is to measure precisely the chemical composition of variously oxidized parts in a titanomagnetite grain using an advanced technique of EPMA. Another objective is to clarify the processes of low-temperature oxidation. Migration of cations in each grain associated with low-temperature oxidation will be considered.

2. Samples and experimental procedures

2.1. Samples

The following samples were selected: (1) titanomagnetites large enough for EPMA analysis (> 10 μm); (2) titanomagnetites without exsolution ilmenite lamellae, because exsolution seems to be an indication of high-temperature oxidation; and (3) titanomagnetites with various Fe and Ti contents in different kinds of volcanic rocks, because one of the processes of chemical change in titanomagnetites may depend on the initial Fe and Ti contents.

The samples were collected from different localities and their magnetic properties are shown in Table 1. Sample A from Kumejima Island, Ryukyu, is classified as a basaltic andesite and has an age of about 5.5 Ma [16]. Sample B collected at the southern part of the Izu Peninsula, central Japan, is andesite with age of about 7 Ma [17]. Sample C was collected at the Daruma volcano, northwestern part of the Izu Peninsula. This region has suffered from a high degree of hydrothermal alteration between the Pliocene and early Pleistocene [18]. This sample is an andesitic rock with an age estimated as 0.8 Ma (I. Kaneoka, personal com-

TABLE 1

Summary of magnetic properties of samples

Sample	Sampling site	Thermal analysis				Visual observation				Reference [g]
		J_s (emu/g)	T_c (°C)	type [a]	J_h/J_0 [b]	size [c] (μm)	degree [d]	crack [e]	boundary [f]	
A	Kume Island	1.16	390	I_2	0.66	250	m	r	c	1
B	Irouzaki	1.29	380	I_1	1.34	220	m	r	c	2
C	Daruma volcano	1.66	440	I_2	0.53	200	m	r	c	3
D	443-57-1, 6–7	0.31	335	I_1	4.07	110	m	r	c	4
E	443-54-3, 125–127	–	230	I_1	4.16	210	m	a ~ c	n	4
F	443-58-1, 61–63	–	410	I_1	2.00	55	h ~ m	r	r	4
G	443-56-3, 120–122	–	280	I_1	3.50	60	m	r	r	4
H	446A-4-2, 44–46	1.42	280	I_1	1.37	120	s	r ~ n	n	4

[a] Thermomagnetic curves of these samples show two types; one is irreversible with high saturation magnetization after heating (I_1), another is irreversible with lower saturation magnetization after heating (I_2) (Fig. 1).

[b] The ratio of saturation magnetization before heating (J_0) and after heating (J_h).

[c] Average grain size of the largest ten titanomagnetite grains in a thin section.

[d] Oxidation degree: h = high m = middle, s = scarce.

[e] Crack development: a = abundant, c = common, r = rare, n = not detected.

[g] References: 1 = Nakagawa and Murakami [16]; 2 = Kaneoka et al. [17]; 3 = I. Kaneoka (personal communication); 4 = Furuta et al. [19].

munication). These three samples were produced by subaerial eruptions. Samples D through H were recovered from DSDP holes 443 and 446, Leg 58, in the central part of the Shikoku Basin. The basement rocks of hole 443 consist of pillow and massive flow basalts. Samples from holes 443 and 446 are from different flow units [19]. The age of basement rocks of hole 443 is about 17 Ma [20], whereas the rocks from hole 446 are about 50 Ma old [21].

2.2. *Experimental procedures*

Polished thin sections were examined by microscope under polarized and reflected lights. The thermomagnetic analysis was carried out on all samples in a magnetic field of 4.5 kOe. The specimens were heated and cooled in a vacuum of 10^{-3} Pa at a heating and cooling rate of 6°C/minute. Several specimens were heated to 800°C and kept at the maximum temperature for a certain time duration to examine the changes of saturation magnetization during the heating. Typical thermomagnetic curves are shown in Fig. 1.

Prior to chemical analysis, the backscattered electron images (BEI) of titanomagnetite observed using devices installed with the EPMA system and points of analysis were determined.

Chemical analysis was carried out with an automatic 4-channel EPMA (JXA-733, JEOL) connected to a computer performing a standard correction on-line by the ZAF method in which the true concentration is theoretically calculated by correcting the atomic number, absorption and X-ray fluorescence effects on the intensity of X-ray. Accelerating voltage of the instrument was 15 kV

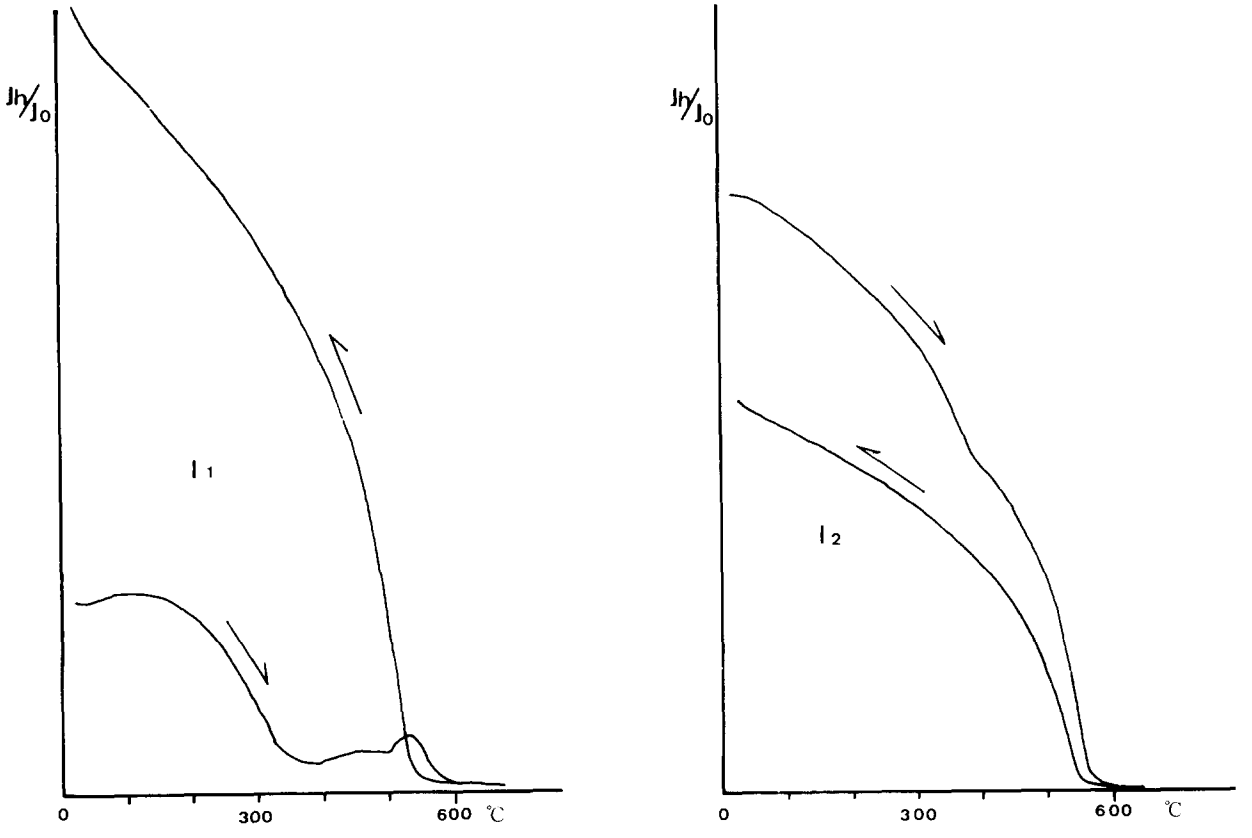

Fig. 1. Typical thermomagnetic curves of sample D (left) recovered from DSDP Site 443 (I_1) and sample A (right) collected from the Kumejima Island (I_2). Samples were heated in vacuum of 10^{-3} Pa and with magnetic field of 4.5 kOe.

and the beam current on the Faraday cup was 20 nA. In all cases in the present experiment nine elements (Fe, Ti, Al, Mg, Mn, Cr, V, Ni, Si) were analyzed.

3. Results

3.1. Microscopic observation

Microscopic observations enable us to identify low-temperature oxidation at the margins of the titanomagnetite and in some cases along cracks within the grains. The oxidation states and microscopic characteristics are described in Table 1. The degree of oxidation was classified on the basis of three microscopic characteristics: color change, crack development in titanomagnetite, and red-colored staining in the surrounding silicates. The color of unoxidized titanomagnetite is brownish gray, whereas that of the oxidized grains is brighter and light gray. Curvilinear cracks within titanomagnetite grains, presumably associated with the volume change of grains during oxidation [22–24], generally tend to increase with progressive degree of oxidation. Pronounced cracks were not detected by the microscope in several grains although they appeared to be oxidized to some extent. Submicroscopic cracks were detected in BEI of these grains. Red staining in silicates and glasses, which implies migration of Fe^{3+} out of titanomagnetite crystals, increases with progressive degree of oxidation [2,24].

In addition to identifying the oxidation stages, the optical anisotropies of titanomagnetite grains were examined. It was shown from this examination that all the grains possess the spinel phase of the magnetite-ulvospinel series β or their oxidized states γ and have no exsolution lamellae of the ilmenite-hematite series (rhombohedral phase α).

3.2. Backscattered electron image (BEI) observation

The BEI technique is similar to the scanning electron microscopy (SEM). The former uses backscattered electrons, while the latter uses the secondary emission from the specimen. BEI image contrast is based on the difference in the total atomic weight of a target (i.e., that in the mean atomic number) and is useful for the examination of the microscopic inhomogeneity in cation distri-

Fig. 2. (a) BEI photograph of grain 1 in sample A. White part is the β phase and slightly dark part on the left hand is the $\gamma 1$ phase. Dark parts between the β and $\gamma 1$ phases and along cracks are the $\gamma 2$ phase. Note that the $\gamma 2$ phase cannot be distinguished from the cavities in this figure. The bar is 50 μm long. (b) BEI photograph taken at a different suppression level of the energy source of the electron beam compared to Fig. 2a. In this figure, though the contrast of β-$\gamma 1$ boundaries is obscure, the $\gamma 2$ phase is distinct. Fine cracks are clearly observed in the $\gamma 2$ phase. The $\gamma 2$ phase develops well along β-$\gamma 1$ boundaries. The bar is 50 μm long.

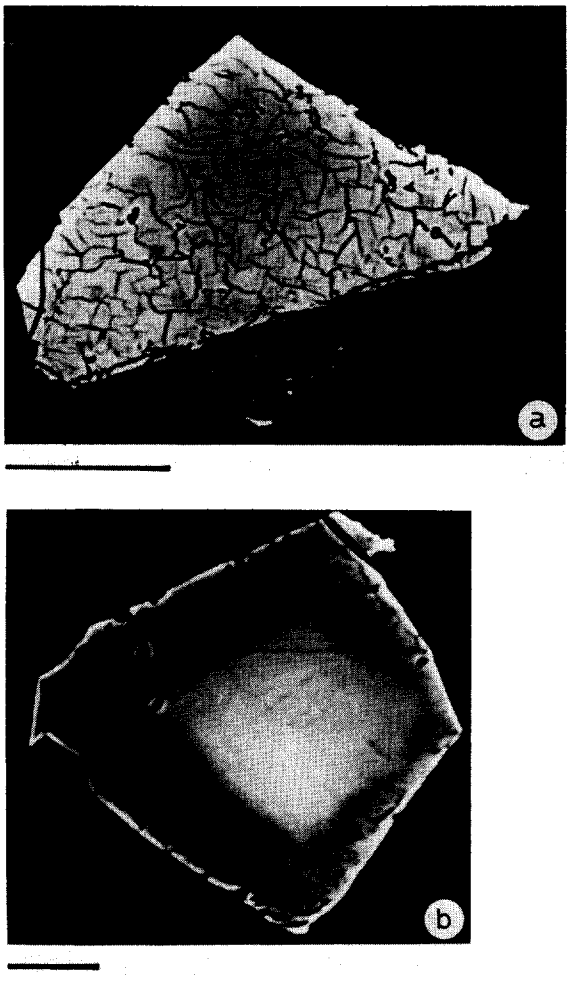

Fig. 3. (a) BEI photograph of oxidized titanomagnetite grain in sample H. Fine physical cracks develop well uniformly. This grain might be oxidized slowly under constant oxidation conditions. The bar is 50 μm long. (b) BEI photograph of the grain in sample D. Chemical cracks are remarkable, while physical cracks do not seem to develop in this grain. The β phase survives at the grain center. The phase boundaries exist at semi-equal distances from the rim of the grain. The phase boundaries look like saw-teeth edged by chemical cracks. The brighter rim does not show the β phase but the edge effect caused by bursting electrons. The bar is 10 μm long.

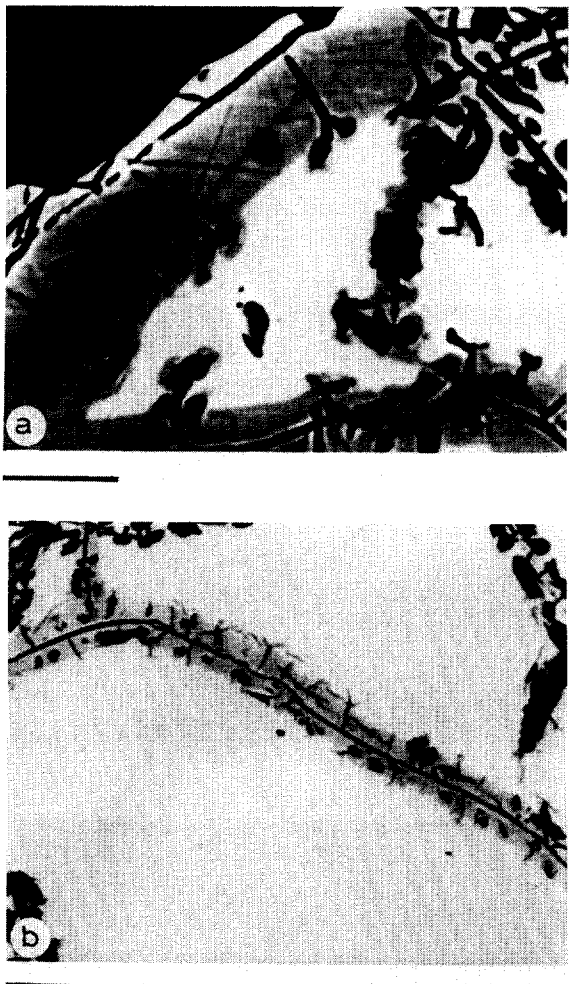

Fig. 4. (a) BEI photograph of a part of partially oxidized grain in sample A. Fine cracks seem to be developing from the rim to the β-γ1 boundary. The directions of crack development are almost perpendicular to the phase boundary and the crack edges at the boundary tend to branch along the boundary. At these branching area, γ2 phases develop and make the seed-leaf-shaped structure. The bar is 10 μm long. (b) BEI photograph of a central part of the oxidized grain in sample A. The γ1 phase develops along pre-existing cracks. Fine cracks develop perpendicular to the pre-existing cracks. The bar is 10 μm long.

bution. The image contrast in brightness is clearly shown in one crystal (Fig. 2). In BEI photomicrographs of titanomagnetite grains, the brighter parts represent the unoxidized phase and the darker ones represent the oxidized one.

Based upon the BEI observation with a high power of image resolution, two schemes regarding the formation of the γ phase and cracks will be proposed. First, the γ phase is divided into two subphases though they could only be detected as one phase under the microscope. They are to be

distinguished by the terms "γ1 phase" and "γ2 phase". The γ1 phase is moderately oxidized, the γ2 phase represents highly oxidized material. Secondly, the cracks within the grain are divided into two groups based on their properties. One is due to the shrinking of the grain volume caused by low-temperature oxidation (Fig. 3a). This type of crack is named "physical crack" hereafter and is similar to the "shrink crack" of Petersen et al. [3]. In some cases these cracks can be identified under high magnification by microscope. The other, which is probably due to the migration of cations within a narrow peripheral area of a grain, can only be detected by BEI (Fig. 3b). This crack is called "chemical crack" hereafter. It is suggested that the chemical cracks grow with increasing

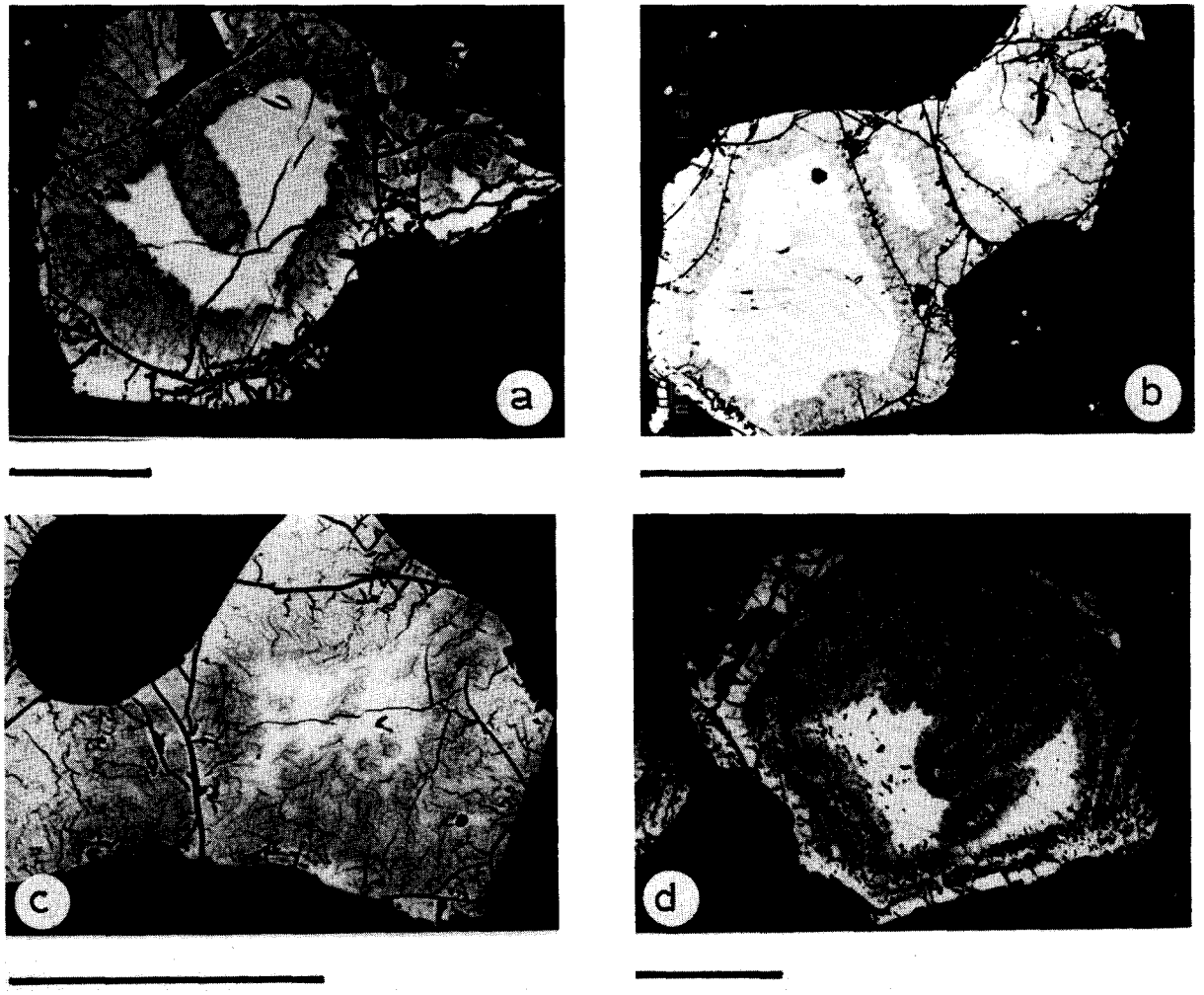

Fig. 5. Examples of BEI photograph of partially oxidized titanomagnetite grains. (a) BEI photograph of grain 2 in sample B. In the γ phase, fine irregular cracks develop and phase boundary is enclosed by fine chemical cracks forming an erosion or oxidation front. The bar is 50 μm long. (b) BEI photograph of the oxidized grain in sample B. The phase boundary is jagged and the γ phase is also filled with fine cracks. The brighter part within the β phase is sulfide mineral (pyrite) included by titanomagnetite. The bar is 100 μm long. (c) BEI photograph of the partially oxidized titanomagnetite in sample B. The β phase does not usually survive. When grain 2 becomes further oxidized, it shows up like this grain. The bar is 50 μm long. (d) BEI photograph of the oxidized grain in sample C which shows concentric shaped γ phases enclosed by cracks and cavities. This structure may be produced by periodically hydrothermal circulation. The bar is 50 μm long.

oxidation and may eventually form a physical crack.

The crack development is observed in Fig. 4. Typical BEI photomicrographs of a titanomagnetite grain in sample A is shown in Fig. 2a and b. The image contrast in brightness is clearly seen in the crystal shown in this figure. The highly oxidized part cannot easily be distinguished from the cavities and cracks in the grain by the image contrast in Fig. 2a. However, it can be identified in Fig. 2b which, compared to Fig. 2a, is taken under different conditions in the suppression level of the electron beam. Examples of BEI photomicrographs of other samples are presented in Fig. 5 which show how low-temperature oxidation proceeds in nature. The internal structure of the grains in sample B (Fig. 5a, b, c) suggests that oxidation gradually proceeds from rim to core of the grain with cracks developing. However, the internal structure of the grain in sample C (Fig. 5d), which has suffered from hydrothermal circulation, is different from those of grains in sample B. The concentric shaped structure of this grain suggests that oxidation proceeded periodically, which may correspond to the periodical activity of hydrothermal circulation.

3.3 Electron probe microanalysis

More than 10 points on each titanomagnetite grain were analyzed by electron probe microanalyzer. Especially on the grain in which at least two different compositions were detected by BEI, micron-order grid analysis was carried out around their boundaries. From these analyses the line profiles of chemical composition (abbreviated as a line) were obtained on the several grains (Figs. 6–9). Lines 1a and 1b are the line profiles on grain 1 in sample A (Figs. 6 and 7). Line 2 is that on grain 2 in sample B (Fig. 8). Line 4 is that on grain 4 in sample D (Fig. 9). The EPMA data obtained along lines 1a and 4 are listed in Table 2.

In all partially oxidized titanomagnetite grains, a sharp variation in the cation composition (Figs. 6, 7, 8 and 9) was found. It cannot be explained by the heterogeneity formed during the crystallization, because such a variation was not found in unoxidized grains. This fact is quite important and justifies a discussion of the cation movement dur-

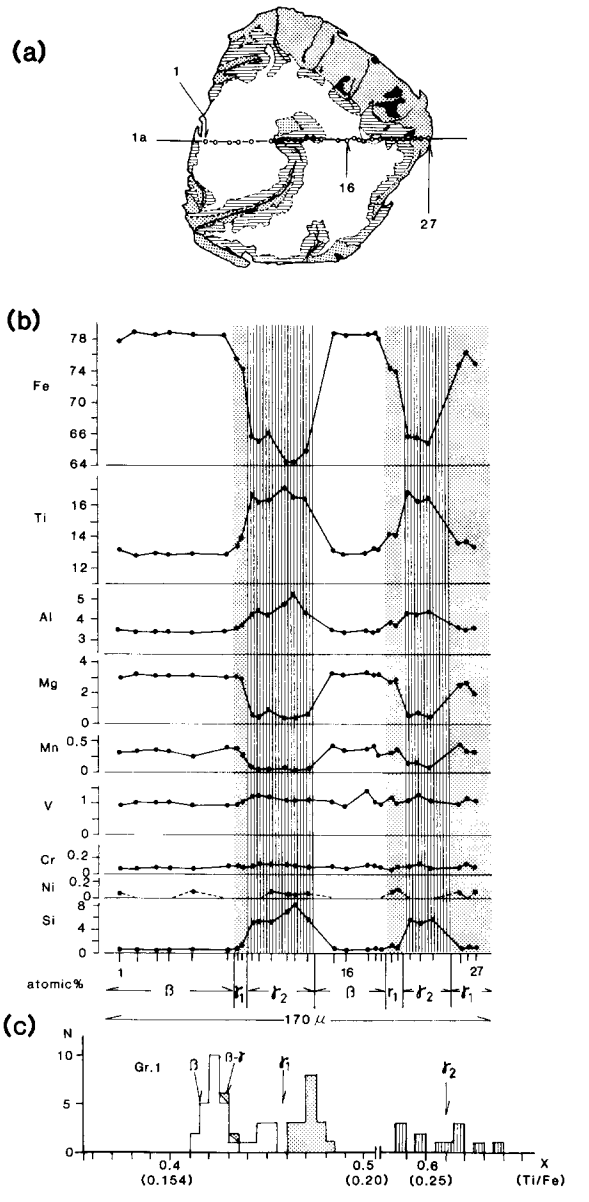

Fig. 6. (a) Illustration of grain 1 in sample A. Gray parts show the γ1 phase and hatched parts, the γ2 phase. Small circles indicated by numbers are the positions of the points analyzed. (b) Line profile along line 1a on grain 1. Gray parts and vertically hatched parts denote γ1 and γ2 phases, respectively. The small numbers beneath the horizontal axis correspond to the points analyzed in the illustration (Fig. 6a) and Table 2. (c) Histogram of variation of the x value for the three phases within grain 1.

TABLE 2

EPMA data obtained along line 1a (grain 1) and line 4 (grain 4)

	Sample A, grain 1														
	1	2	3	4	5	6	7	8	9	10	11	12	13	14	15
SiO_2	0.35	0.08	0.08	0.08	0.09	0.10	0.21	0.61	3.88	3.70	3.64	5.07	6.30	4.24	0.09
TiO_2	14.16	13.87	13.98	13.87	13.91	13.88	14.43	14.86	17.68	17.16	17.34	18.15	17.35	17.47	14.06
FeO*	75.66	77.14	76.74	76.99	76.78	76.69	73.80	72.42	63.99	63.15	63.97	60.51	60.24	61.91	77.09
Al_2O_3	2.53	2.45	2.44	2.47	2.43	2.45	2.59	2.67	3.06	3.15	2.98	3.26	3.71	3.05	2.48
MgO	1.51	1.67	1.55	1.58	1.55	1.55	1.51	1.51	0.27	0.21	0.46	0.19	0.18	0.29	1.62
MnO	0.30	0.35	0.34	0.32	0.29	0.38	0.35	0.28	0.06	–	0.04	0.05	–	–	0.38
V_2O_3	0.92	1.02	1.01	1.01	0.94	0.93	0.94	1.01	1.17	1.23	1.13	1.04	1.04	1.09	0.99
Cr_2O_3	0.09	0.06	0.08	0.07	0.08	0.09	0.09	0.08	0.08	0.11	0.12	0.10	0.10	0.06	0.06
NiO	0.04	–	–	–	0.06	–	–	–	–	–	0.07	0.05	0.03	0.02	–
Total	95.55	96.59	96.22	96.38	96.14	96.06	93.92	93.44	90.17	88.71	89.75	88.41	88.94	88.13	96.78
Cation ratio															
Si	0.013	0.003	0.003	0.003	0.004	0.004	0.008	0.023	0.153	0.149	0.145	0.204	0.251	0.171	0.003
Ti	0.397	0.384	0.389	0.385	0.387	0.387	0.411	0.425	0.527	0.519	0.517	0.549	0.520	0.531	0.388
Fe*	2.357	2.374	2.374	2.376	2.376	2.375	2.338	2.304	2.120	2.122	2.126	2.036	2.006	2.094	2.368
Al	0.111	0.106	0.106	0.107	0.106	0.107	0.115	0.119	0.143	0.149	0.140	0.155	0.174	0.145	0.107
Mg	0.084	0.089	0.085	0.087	0.086	0.085	0.085	0.086	0.016	0.013	0.027	0.011	0.011	0.017	0.089
Mn	0.009	0.011	0.011	0.010	0.009	0.012	0.011	0.009	0.002	–	0.001	0.002	–	–	0.012
V	0.028	0.030	0.029	0.030	0.028	0.027	0.029	0.031	0.037	0.040	0.036	0.034	0.033	0.035	0.029
Cr	0.003	0.002	0.002	0.002	0.003	0.003	0.003	0.003	0.003	0.003	0.004	0.003	0.003	0.002	0.002
Ni	0.001	–	–	–	0.002	–	–	–	–	–	0.002	0.002	0.001	0.001	–
Ti/Fe	0.168	0.162	0.164	0.162	0.163	0.163	0.176	0.184	0.248	0.244	0.244	0.270	0.259	0.254	0.164
x	0.432	0.418	0.423	0.418	0.420	0.420	0.449	0.466	0.596	0.588	0.588	0.638	0.617	0.608	0.423
Ti/R	0.153	0.147	0.149	0.147	0.148	0.148	0.159	0.167	0.227	0.223	0.222	0.245	0.233	0.232	0.149
x'	0.398	0.384	0.389	0.384	0.387	0.387	0.412	0.429	0.555	0.547	0.545	0.590	0.567	0.565	0.384

TABLE 2 (continued)

	Sample A, grain 1 (continued)											
	16	17	18	19	20	21	22	23	24	25	26	27
SiO_2	0.08	0.13	0.15	0.12	0.75	0.26	4.03	3.36	4.09	0.15	0.07	0.14
TiO_2	13.84	13.93	14.17	14.13	15.11	14.99	17.89	17.10	17.47	14.45	14.52	14.33
FeO*	76.37	76.61	76.60	76.29	72.21	72.16	63.03	63.51	63.00	72.97	74.53	72.88
Al_2O_3	2.45	2.46	2.42	2.46	2.71	2.63	3.04	2.99	3.07	2.54	2.49	2.58
MgO	1.52	1.57	1.51	1.53	1.33	1.40	0.22	0.31	0.16	1.24	1.26	0.90
MnO	0.30	0.34	0.39	0.24	0.28	0.37	0.10	0.09	0.03	0.41	0.29	0.29
V_2O_3	0.84	1.39	0.96	0.94	1.11	0.94	1.05	1.27	1.05	0.94	1.06	1.05
Cr_2O_3	0.04	0.09	0.09	0.06	0.04	0.07	0.07	0.10	0.06	0.05	0.11	0.04
NiO	–	–	–	–	0.02	0.07	–	–	–	0.02	–	0.05
Total	95.44	96.50	96.27	95.77	93.55	92.90	89.43	88.73	88.91	92.76	94.33	92.26
Cation ratio												
Si	0.003	0.005	0.006	0.004	0.029	0.010	0.160	0.135	0.164	0.005	0.003	0.006
Ti	0.388	0.386	0.394	0.395	0.432	0.432	0.536	0.517	0.528	0.418	0.413	0.418
Fe*	2.381	2.362	2.367	2.371	2.298	2.313	2.099	2.136	2.116	2.347	2.357	2.362
Al	0.108	0.107	0.105	0.108	0.121	0.119	0.143	0.142	0.145	0.115	0.111	0.118
Mg	0.084	0.086	0.083	0.085	0.075	0.080	0.013	0.019	0.010	0.071	0.071	0.052
Mn	0.009	0.011	0.012	0.008	0.009	0.012	0.003	0.003	0.001	0.013	0.009	0.009
V	0.025	0.041	0.028	0.028	0.034	0.029	0.034	0.041	0.034	0.029	0.032	0.033
Cr	0.001	0.003	0.002	0.002	0.001	0.002	0.002	0.003	0.002	0.001	0.003	0.001
Ni	–	–	–	–	0.001	0.002	–	–	–	0.001	–	0.001
Ti/Fe	0.163	0.164	0.166	0.167	0.188	0.187	0.255	0.242	0.249	0.178	0.175	0.177
x	0.423	0.423	0.427	0.429	0.475	0.473	0.610	0.585	0.598	0.453	0.447	0.451
Ti/R	0.149	0.148	0.152	0.152	0.170	0.169	0.233	0.221	0.229	0.162	0.160	0.162
x'	0.384	0.387	0.396	0.396	0.436	0.434	0.567	0.543	0.559	0.418	0.414	0.418

TABLE 2 (continued)

	Sample D, grain 4														
	177	178	179	180	181	182	183	184	185	186	187	188	189	190	191
SiO_2	0.68	0.67	0.63	0.12	0.10	0.11	0.09	0.14	0.87	0.72	0.74	0.77	0.71	0.80	0.56
TiO_2	20.99	20.97	21.18	19.12	19.19	18.91	18.91	19.03	20.23	20.18	20.37	21.47	21.03	21.45	20.48
FeO*	64.34	64.51	65.00	70.76	71.47	71.86	72.28	71.28	65.09	65.22	65.61	63.86	62.64	64.26	64.76
Al_2O_3	2.28	2.22	2.41	2.47	2.51	2.52	2.48	2.47	2.16	2.20	1.96	2.17	2.26	2.10	2.45
MgO	1.14	0.97	1.03	1.19	1.12	1.23	1.17	1.22	1.07	1.17	0.98	0.93	1.07	0.85	0.94
MnO	0.61	0.60	0.58	0.61	0.57	0.62	0.61	0.59	0.61	0.64	0.56	0.58	0.59	0.58	0.61
V_2O_3	0.71	0.69	0.63	0.76	0.73	0.82	0.81	0.72	0.84	0.69	0.77	0.71	0.73	0.66	0.82
Cr_2O_3	0.07	0.03	0.09	0.04	0.04	0.05	0.05	0.05	0.04	0.05	0.05	0.01	0.07	0.04	0.09
NiO	0.04	0.01	–	–	0.06	–	–	–	0.02	0.01	0.02	0.06	0.01	0.01	–
Total	90.87	90.66	91.57	95.07	95.79	96.10	96.41	95.49	90.95	90.88	91.06	90.57	89.11	90.84	90.72
Cation ratio															
Si	0.027	0.027	0.025	0.005	0.004	0.004	0.003	0.005	0.034	0.028	0.029	0.030	0.029	0.032	0.022
Ti	0.624	0.626	0.625	0.542	0.540	0.530	0.529	0.537	0.601	0.600	0.606	0.641	0.638	0.639	0.611
Fe*	2.132	2.140	2.134	2.233	2.238	2.241	2.249	2.238	2.151	2.155	2.170	2.120	2.114	2.131	2.148
Al	0.106	0.104	0.116	0.110	0.111	0.111	0.109	0.109	0.101	0.103	0.092	0.102	0.107	0.098	0.114
Mg	0.067	0.057	0.060	0.067	0.062	0.068	0.065	0.068	0.063	0.069	0.058	0.055	0.065	0.050	0.055
Mn	0.020	0.020	0.020	0.019	0.018	0.020	0.019	0.019	0.020	0.021	0.019	0.019	0.020	0.020	0.021
V	0.022	0.022	0.020	0.023	0.022	0.025	0.024	0.022	0.027	0.022	0.024	0.023	0.024	0.021	0.026
Cr	0.002	0.001	0.003	0.001	0.001	0.001	0.001	0.002	0.001	0.003	0.002	–	0.002	0.001	0.003
Ni	0.001	–	–	–	0.002	–	–	–	0.001	–	0.001	0.002	–	–	–
Ti/Fe	0.293	0.292	0.293	0.243	0.241	0.237	0.235	0.240	0.279	0.278	0.279	0.302	0.302	0.300	0.284
x	0.680	0.678	0.680	0.586	0.583	0.575	0.571	0.581	0.654	0.653	0.654	0.696	0.696	0.692	0.664
Ti/R	0.266	0.267	0.266	0.221	0.220	0.215	0.214	0.219	0.254	0.253	0.256	0.276	0.274	0.276	0.258
x'	0.630	0.632	0.630	0.543	0.541	0.531	0.529	0.539	0.608	0.606	0.611	0.649	0.645	0.649	0.615

Numbers correspond to the analyzed points in Figs. 6 and 9. FeO* and Fe* represent total iron oxide as FeO and total iron as Fe^{2+}. Cation ratios are calculated assuming stoichiometry. The x values and Ti/Fe ratios were calculated on the assumption that the minor cations Al, Mg, Mn, V, Cr and Ni sneak in other spinel solid solution with titanomagnetite. The x' values and Ti/R ratios are derived on the assumption that the minor elements substitute for Fe in the titanomagnetite lattice.

ing low-temperature oxidation. The line profiles on the partially oxidized grains generally indicate the following variations in cation compositions.

(1) Fe^{2+} or Fe^{3+} and the divalent cations such as Mg^{2+} and Mn^{2+} tend to decrease in the oxidized parts. In slightly oxidized states, Fe cations begin to decrease simultaneously as the oxidation begins. On the other hand, the other divalent cations do not seem to move at this oxidation state (line 1b in Fig. 7). This delay of the cation motion may depend on their diffusion (or migration) rates. In the highly oxidized states such as the $\gamma 2$ phase on line 1a, both Fe and the divalent cations decrease substantially (Fig. 6).

(2) Ti^{4+} and the trivalent cations such as Al^{3+} and V^{3+} tend to increase in the oxidized parts. The variations of Al^{3+} and V^{3+} contents are less remarkable than that of Ti^{4+} content but their changes seem to occur in the same regions as those in which Ti^{4+} content begins to increase. The difference in behavior between Ti^{4+} and the trivalent minor cations may not depend on the difference of their diffusion rates but on the difference of their primary amounts. The increase of these cations seems to be remarkable as the oxidation proceeds. Other minor divalent and trivalent cations such as Ni^{2+} and Cr^{3+} are rarely found in titanomagnetite and its oxidized phase.

(3) In general, the SiO_2 content of titanomagnetite is usually less than 0.2% in weight and the abundance of SiO_2 has been only used to test the correct position of the electron beam on the

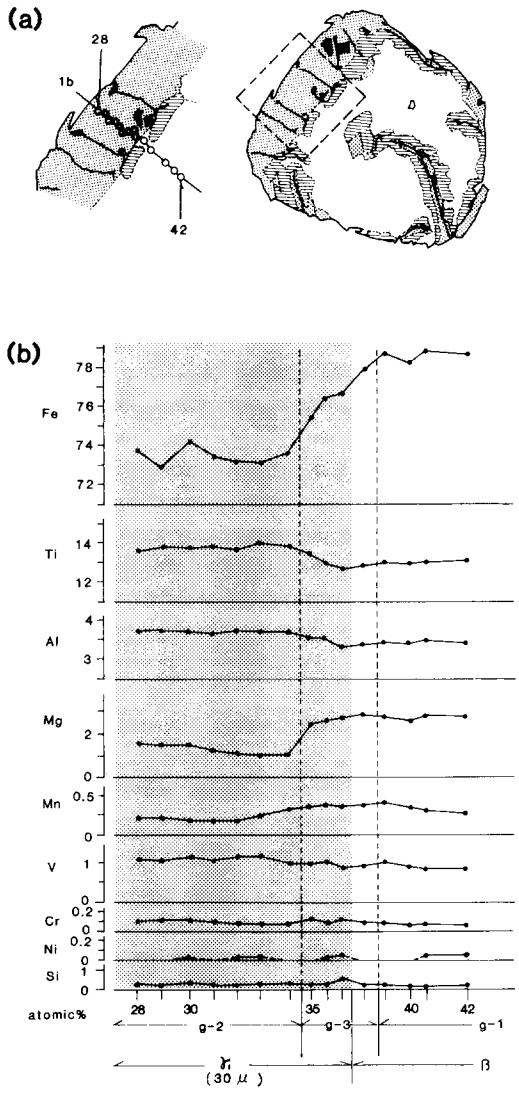

Fig. 7. (a) Illustration of grain 1 (right) in sample A showing the position of line 1b. The part enclosed by broken line is enlarged and shown on the left side of the figure. (b) Line profile (line 1b) on grain 1. Group 1 (g-1) is the β phase, group 2 (g-2) is the γ1 phase and group 3 (g-3) is the β-γ transition zone. FeO* contents tend to decrease in g-3 but the contents of other divalent metal oxides such as MgO and MnO decrease near the boundary between g-2 and g-3.

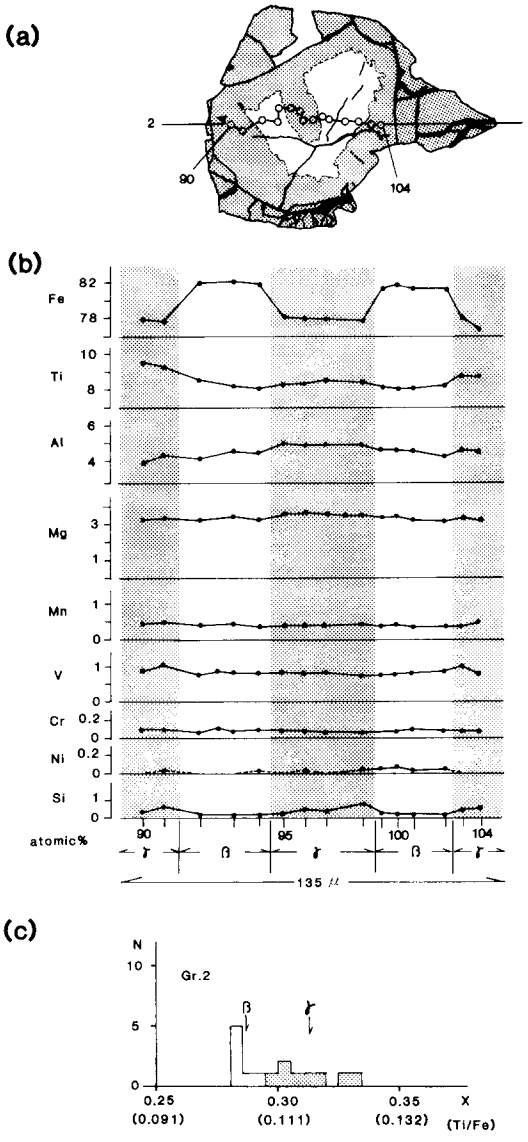

Fig. 8. (a) Illustration of grain 2 in sample B. Gray parts represent the γ phase. The β phase resides in the horse-shoe shaped area. (b) Line profile (line 2) on grain 2. Gray parts denote the γ phase and small numbers beneath the horizontal axis correspond to the numbers of the points analyzed in Fig. 8a. Alhough the normal zoning of titanomagnetite generally shows an increase in Ti contents and decrease in Fe contents from core to rim, a sharp decrease in Fe contents of the γ phase at the central part of the grain is observed. (c) Histogram showing the variation of x of the β and γ phases within grain 2.

grain [3]. However, in the present study Si^{4+} cations tend to increase with progressive oxidation (line 1a in Fig. 6). This observation suggests that low-temperature oxidation causes replacement of elements such as Si^{4+} in the surrounding silicates. The replacement of Si^{4+} should not be due to solid diffusion because the diffusion rate of Si in solid is a thousand times smaller than that of Fe

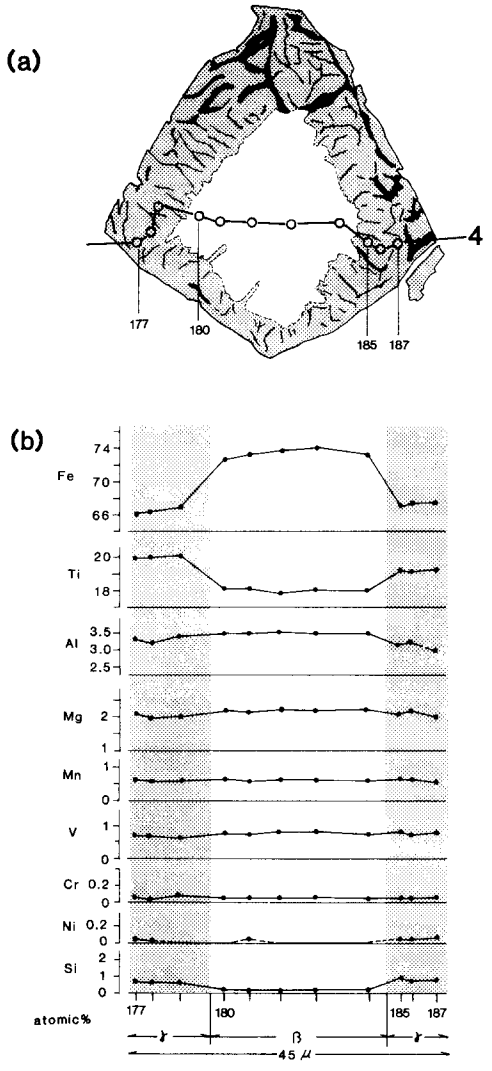

Fig. 9. (a) Illustration of grain 4 in sample D showing the positions of the points analyzed and the line profile (line 4). Fine black curves distributed in the γ phase are the chemical cracks. (b) Line profile (line 4) on grain 4.

[25]. The enrichment of Si^{4+} thus seems to be carried by the accretion of hydrocirculative materials.

The behavior of the individual cations are due to low-temperature oxidation because the chemical composition of unoxidized grain is nearly homogeneous except for some heterogeneity produced during crystallization limited to the grains rims [26]. The zoning in the grain rim is considered to be a normal phenomenon produced on cooling. In normal zoning the Fe, Al and Mg contents decrease and Ti, Mn and V contents increase from core to grain edge.

In contrast to chemical homogeneity in each grain, variation in chemical composition among grains is found even in one sample. Therefore, chemical composition between β and γ phases cannot be compared using different grains even in one sample when the compositional change by the oxidation is examined.

4. Discussion

4.1. Oxidation processes and changes in chemical composition

4.1.1. Primary composition of titanomagnetite

Titanomagnetite is a member of the solid solution series between magnetite and ulvospinel, which is defined by the x value in the relationship $Fe_{3-x}Ti_xO_4$. The x values of titanomagnetites prior to low-temperature oxidation in submarine basalts are concentrated in a narrow range around $x = 0.6$ [2,10]. Present results show, however, that the x value of some titanomagnetites in submarine basalt samples D through H, varies from 0.46 to 0.60 (Fig. 10). Such a variation was also reported in other DSDP samples by Steiner [14] and Furuta [15]. The variation in x depends mainly on the bulk composition of rock samples and on the thermal and geochemical environment during cooling.

The present results on the primary composition of titanomagnetite imply important problems. Most of the previous investigators have studied the compositional change with low-temperature oxidation by comparing the compositions of different grains oxidized to various degrees on an assumption that the primary compositions of these grains are roughly identical [2,10]. It is unlikely that this assumption is always valid in submarine basalts.

The variation of the x values within one titanomagnetite grain is very small (e.g., grain 4 in Fig. 10). The homogeneity in composition within one grain can be attributed to the homogenization by diffusion of individual cations in solid state at high temperatures. Heterogeneity in composition

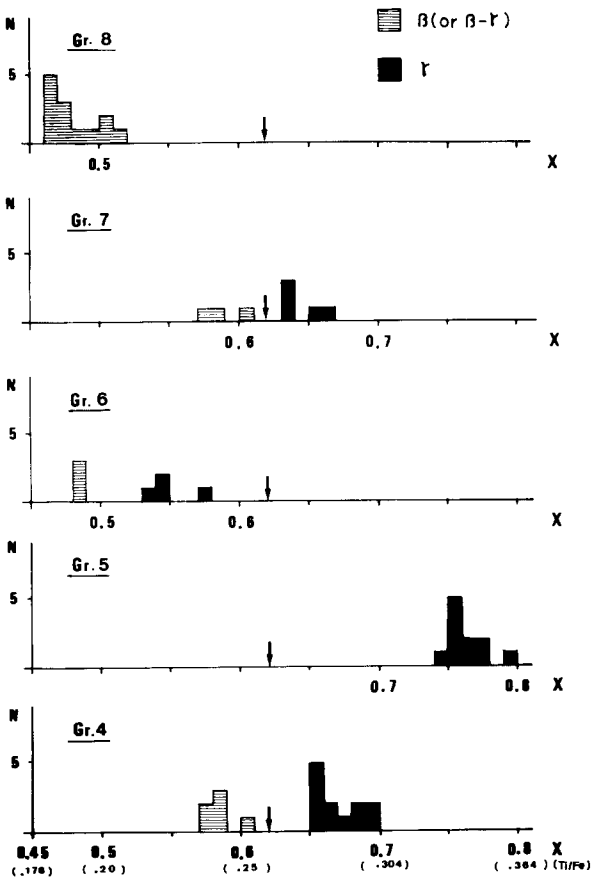

Fig. 10. Histogram showing the variation of x of titanomagnetites in submarine basalts. The arrows show the typical x value of titanomagnetite in ocean floor basalts as reported by Johnson and Hall [2] ($x = 0.625$).

within one grain may be produced by crystallization differentiation but it can quickly be eliminated by rapid diffusion of metal ions. The homogenization becomes suppressed as the materials cool since the diffusion rate depends exponentially on temperature. Probably homogenization rarely occurs after the end of crystallization.

4.1.2. Oxidation path on the ternary diagram

Two models have been proposed for low-temperature oxidation. One assumes that low-temperature oxidation is simple oxidation with only the addition of oxygen to the pre-exsiting crystals [8,13] which can be expressed by the following equation:

$$Fe^{2+} + (z/2)O \rightarrow (1-z)Fe^{2+} + zFe^{3+} + (z/2)O^{2-} + (3z/8)\square \quad (1)$$

where z is the oxidation parameter defined by O'Reilly and Banerjee [5], $\square$ is the lattice vacancy to maintain the charge balance in the lattice.

The other model assumes that Fe^{2+} (or Fe^{3+}) migrates out of the titanomagnetite lattice during low-temperature oxidation [2,3,10,12] which can be expressed by the following equation:

$$Fe^{2+} \rightarrow (1-z)Fe^{2+} + (2z/3)Fe^{3+} + (z/3)\square + [(2z/3)e^{-} + (z/3)Fe^{2+}] \quad (2)$$

or:

$$Fe^{2+} \rightarrow (1-z)Fe^{2+} + (2z/3)Fe^{3+} + (z/3)\square + [ze^{-} + (z/3)Fe^{3+}] \quad (3)$$

The last parenthesized terms of equations (2) and (3) denote Fe cations migrating out of the lattice.

The oxidation path on the ternary diagram for Fe-Ti oxide minerals was determined from EPMA data in order to examine the oxidation models mentioned above, because each of these models has a unique oxidation path. If low-temperature oxidation is the simple process expressed as equation (1), the oxidation path should be parallel to the base line of the ternary diagram, which corresponds to equi-Ti/R ratio line, where R is the detected constituent cations exclusive of Ti and Si. If the oxidation is accompanied by cation migration, the path has a slope upward from left to

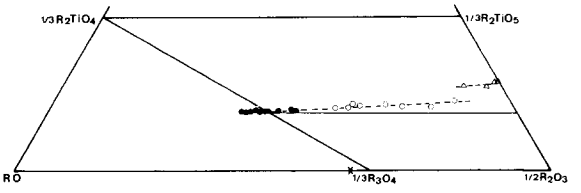

Fig. 11. Ternary diagram projection of EPMA data of β, $\gamma 1$ and $\gamma 2$ phases of grain 1. Solid circle, open circle and triangle represent β, $\gamma 1$ and $\gamma 2$ phases, respectively. Solid lines within the $\frac{1}{3}R_2TiO_4$-$\frac{1}{3}R_3O_4$-$\frac{1}{2}R_2O_3$-$\frac{1}{3}R_2TiO_5$ quadrangle are the equi-Ti/R ratio (Ti/R = 0.15) line. Broken lines represent the fit to plotted data points of apparent oxidation path. Cross mark on the RO-$\frac{1}{2}R_2O_3$ line is the calibration data of synthesized magnetite.

right, which corresponds to equi-Ti/O ratio line as proposed by Petersen et al. [3].

Since the starting material (unoxidized titanomagnetite) is homogeneous, the oxidation path can be determined by plotting the composition of β and γ parts within one grain (Fig. 11). The EPMA data were plotted on the ternary diagram based upon the following assumptions:

(1) As the minor cations are considered to substitute for some of the Fe cations within the titanomagnetite lattice [3,12,14,27], the chemical composition determined by EPMA analysis is plotted on the ternary diagram of TiO_2-RO-$\frac{1}{2}R_2O_3$, where R represents the divalent or trivalent cations including Fe^{2+} and Fe^{3+} which all constitute the titanomagnetite lattice.

(2) The amount of Fe^{3+} is estimated on an assumption that cations constituting a titanomagnetite crystal are composed of the only nine elements analyzed by present EPMA analyses plus oxygen combined with them, which is confirmed by the energy-dispersive spectroscopy (EDS) method. Iron is usually assumed to occur as FeO. The difference of weight percent EPMA data from 100 is, therefore, equal to the amount of oxygen combined with Fe^{3+} cations. This allows Fe^{3+} abundances to be estimated. In the highly oxidized $\gamma 2$ phase, the difference of total weight percent EPMA data from 100 does not always correspond to the amount of Fe^{3+} content, because of microcracks and cavities caused by progressive oxidation which exist at the highly oxidized parts. Only EPMA data of highly oxidized parts where the electron beam does not emit the microcracks and cavities are, therefore, plotted on the diagram (Fig. 11).

The oxidation path obtained shows a slope upward from left to right on the diagram. It strongly supports the idea that low-temperature oxidation is not a simple oxidation but is accompanied by cation migration. A synthesized pure magnetite standard and a natural pure hematite were analyzed immediately after each measurement of the natural grain. The data of these stoichiometric samples are plotted at the accurate positions of magnetite and hematite on the ternary diagram. It indicates that the amount of Fe^{3+} is correctly estimated in our method.

4.1.3. Cation migration during low-temperature oxidation

The migration is caused by the following three processes (1) depletion, (2) enrichment and (3) replacement of cations. The cations of depletion type are Fe^{2+} (Fe^{3+}), Mg^{2+} and Mn^{2+} which show high mobilities and migrate out of the lattice

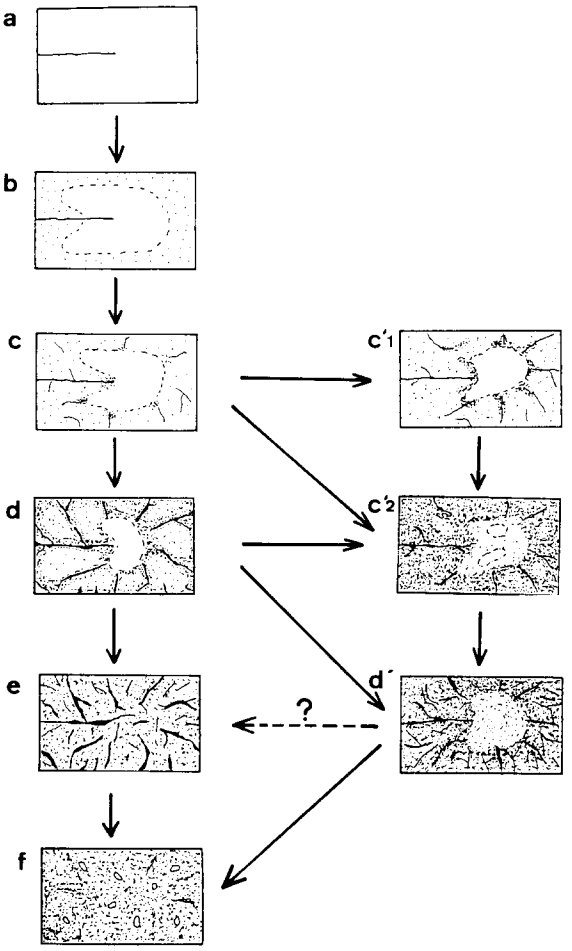

Fig. 12. A schematic diagram of the processes of low-temperature oxidation. Stages *a* through *f* along the vertical column (left) represent the commonly occurring oxidation process where the oxidation condition is nearly constant. When the oxidation is highly activated by hydrocirculation, the process branches to stages *c'1*, *c'2* or *d'*. For example, samples B, E and H correspond to stage *b* and samples A and C correspond to stages *c'1* and *c'2*, respectively. Samples D, F and G correspond to stages *d* or *d'*. Moreover, highly altered titanomagnetite grains which correspond to stage *f* commonly exist in the samples drilled from DSDP Hole 504B, Leg 83.

with progressive oxidation. The migration is probably associated with not only diffusion in solids but also erosion and transportation of cations by hydrocirculation.

Enrichment is caused by differential motion of cations with various mobilities. The cations to be enriched are Ti^{4+}, Al^{3+} and V^{3+} with lower mobilities. They concentrate in the oxidized part of the grain. As the oxidation proceeds, the cations with high mobilities easily migrate out of the lattice but the cations with low mobilities remain within the lattice. When the lattice shrinks by reduction of the cell edge, the concentration of the remaining cations becomes larger.

Si^{4+} is also enriched in the oxidized part, but the mechanism of this enrichment is different from that of other ions. Since Si^{4+} content in unoxidized titanomagnetite lattice is small, the degree of Si^{4+} enrichment by lattice shrinkage is not considerable. Si^{4+} contained in the oxidized part came from the surrounding silicates entering the microcracks and cavities of the grain. Therefore, in this process the cations migrating out of the lattice are replaced by Si^{4+}. The carrier of these cations is probably hydrocirculation which maintains the chemical potential gradient between the lattice and its environment sufficiently steep.

4.2. Internal structures of titanomagnetite after low-temperature oxidation

4.2.1. Crack development

The increase in the cracks associated with low-temperature oxidation is explained as a result of volume decrease of the crystal [12]. The hydrocirculation may erode titanomagnetite crystals along the weak line where internal stress concentrates. Erosion finally produces cracks defined as chemical cracks. The chemical cracks may be traces of transportation passages of cations with water and stimulate low-temperature oxidation. It is shown by BEI observation that extensive physical cracks do not develop simultaneously with the chemical cracks. Development of fine chemical cracks may gradually release the internal stress before it is concentrated enough to form physical cracks. If low-temperature oxidation proceeds gradually without internal erosion by hydrocirculation, the concentration of the internal stress continues until the physical cracks occur.

4.2.2. Change of internal structure with low-temperature oxidation

Internal structure changes of titanomagnetite grains can be traced by BEI (Fig. 12), and they imply that oxidation proceeds according to two processes: the commonly occurring oxidation process and the peculiar process caused by the change of oxidation condition. Oxidation progresses from stage *a* to *f* (Fig. 12) in the commonly occurring process where oxidation conditions such as activity of hydrocirculation or oxidation rate remain nearly constant. When oxidation conditions change, the internal structure of the grain shows the peculiar features (stages *c'1*, *c'2* and *d'*, Fig. 12). In stage *c'1* oxidation proceeds more rapidly at parts open to erosion such as at the crack edges and phase boundaries. These parts become the $\gamma 2$ phase. Unoxidized parts of the grain in stage *c'1* begin to be oxidized in stage *c'2* and eventually the grain is to be devoid of the β phase in stage *d'*. The process of oxidation in stages *c'2* and *d'* seem to be slow and gradual compared to stage *c'1*. In both oxidation processes, the grain finally reaches stage *f* where titanomagnetite dissociates to several minerals such as α-hematite, hydro-oxides and clay minerals.

Cracks divide titanomagnetite grains and make the effective grain size smaller, which causes remanent magnetization to be more stable [12]. This effect may be maintained up to stage *e*. However, remanent magnetization will be destroyed in the final oxidation stage (*f*), because the effective grain size of some subdivided fragments of the grain is smaller than the critical size of stable single domain configuration [12]. Completely oxidized grains in nature may not be in a form of crystal but become amorphous or mixtures of submicron-sized crystals. Since these submicron-sized crystals do not maintain a cubic structure any longer, the grain often shows optical anisotropy under the microscope. In fact, the several grains in DSDP Site 504B basalts show a strongly optical anisotropy, which had suffered from hydrothermal alteration [28].

5. Conclusions

The results obtained in this study lead to the following conclusions.

(1) Although the primary composition of titanomagnetite is variable among individual grains in a rock sample, it is homogeneous in each grain, except for a limited part of the rim of the grain.

(2) The x value increases during low-temperature oxidation. Low-temperature oxidation is not a simple addition of oxygen but is associated with cation migration. Cation migration is observed with most of the constituent elements as follows: (a) Fe, Mg and Mn cations migrate out of the titanomagnetite lattice during oxidation (depletion type); (b) Ti, Al and V cations are enriched during oxidation (enrichment type); (c) Si cations in the surrounding silicates or glasses are added to titanomagnetite during oxidation (replacement type).

Cation migration is due to both diffusion in solids and transportation by hydrocirculation. The former process occurs in all oxidation states, while the latter is predominant in highly oxidized stages and associated with the crack development.

(3) The detailed internal structure of titanomagnetite can be examined by BEI. Cracks developed by low-temperature oxidation are classified into physical and chemical cracks. Chemical cracks are due to the cation migration process. They play an important role as a transportation path of the migrating and replacing cations with water. Physical cracks are due to the shrinking of the crystal volume with oxidation. Several oxidation stages can be traced by change in internal structure of titanomagnetite crystal (Fig. 12).

Acknowledgements

The authors would like to thank K. Kobayashi, K. Kanehira, T. Mori and M. Otsuki for their helpful suggestions and discussions, and also thank P.H. Johnson and S. Halgedahl for their critical reviews of this manuscript.

References

1 M. Marshall, and A. Cox, Magnetic changes in pillow basalts due to sea floor weathering, J. Geophys. Res. 77, 6459–6469, 1972.
2 H.P. Johnson and J.M. Hall, A detailed rock magnetic and opaque mineralogy study of the basalts from the Nazca plate, Geophys. J. R. Astron. Soc. 52, 45–64, 1978.
3 N.P. Petersen, P. Eisenbach and U. Bleil, Low-temperature alteration of the magnetic minerals in ocean floor basalts, in: Deep Drilling in the Atlantic Ocean: Ocean Crust, M. Talwani et al., eds., Am. Geophys. Union, M. Ewing Ser. 2, 169–209, 1979.
4 E. Irving, The Mid-Atlantic Ridge at 45°N. Oxidation and magnetic properties of basalt; review and discussion, Can. J. Earth Sci. 7, 1528–1538, 1970.
5 W. O'Reilly and S.K. Banerjee, Oxidation of titanomagnetite and self-reversal, Nature 211, 26–28, 166.
6 M. Ozima and E.E. Larson, Low- and high-temperature oxidation of titanomagnetite in relation to irreversible changes in the magnetic properties of submarine basalts, J. Geophys. Res. 75, 1003–1017, 1970.
7 M. Ozima and N. Sakamoto, Magnetic properties of synthesized titanomaghemite, J. Geophys. Res. 67, 7035–7046, 1971.
8 P.W. Readman and W. O'Reilly, Magnetic properties of oxidized (cation-deficient) titanomagnetites (Fe, Ti, $\square)_3O_4$, J. Geomag. Geoelectr. 24, 69–90, 1972.
9 M. Ozima, M. Joshima and H. Kinoshita, Magnetic properties of submarine basalts and the implications on the structure of the oceanic crust, J. Geomag. Geoelectr. 26, 335–354, 1974.
10 P.J.C. Ryall and J.M. Hall, Iron loss in titanomagnetites during low temperature oxidation, J. Geomag. Geoelectr. 32, 661–669, 1980.
11 W. Feitknecht and K.J. Gallagher, Mechanism for oxidation of Fe_2O_3, Nature 228, 548–549, 1970.
12 M. Prévot, A. Lecaille and E.A. Mankinen, Magnetic effects of maghemitization of oceanic crust, J. Geophys. Res. 86, 4009–4020, 1981.
13 W. O'Reilly, and S.K. Banerjee, The mechanism of oxidation in titanomagnetites; a magnetic study, Mineral. Mag. 36, 29–37, 1967.
14 M.B. Steiner, An investigation of ulvospinel composition and cation migration during maghemitization in Deep Sea Drilling Project Leg 61 titanomagnetites, J. Geophys. Res. 87, 5361–5374, 1982.
15 T. Furuta, Magnetic properties of basalt samples from Holes 504B and 505B on the Costa Rica Rift, Deep Sea Drilling Project Legs 60 and 70, in : J.R. Cann, Langseth et al. Initial Reports of Deep Sea Drilling Project 69, 711–720, 1983.
16 H. Nakagawa and M. Murakami, Geology of Kume-jima, Okinawa gunto, Ryukyu Islands, Japan, Tohoku Univ. Inst. Geol. Pal. Contrib. 75, 1–16, 1975.
17 I. Kaneoka, S. Aramaki and S. Tonouchi, K-Ar ages of a basanitoid lava flow of Nanzaki Volcano and underlying

Miocene andesites from the Irozaki area, Izu Peninsula, Central Japan, J. Geol. Soc. Jpn. 88, 919–922, 1982.

18 A. Iijima and S. Iwao, Geology of the Ugusu district, western Izu, J. Geol. Soc. Jpn, 76, 591–604, 1970.

19 T. Furuta, K. Kobayashi and K. Momose, Magnetic properties of igneous rocks of the Philippine Sea, in: Klein, Kobayashi et al., Initial Reports of Deep Sea Drilling Project 58, 923–934, 1980.

20 G.V. Klein and K. Kobayashi, Geological summary of the North Philippine Sea based on Deep Sea Drilling Project Leg 58 results, in : G.V. Klein, K. Kobayashi et al., Initial Reports of Deep Sea Drilling Project 58, 951–961, 1980.

21 M. Ozima, Y. Takigami and I. Kaneoka, ^{40}Ar-^{39}Ar geochronological studies on rocks of DSDP Site 443, 445 and 446, in: G.V. Klein, K. Kobayashi et al., Initial Reports of Deep Sea Drilling Project, 58, 917–920, 1980.

22 E.E. Larson and D.W. Strangway, Magnetization of Spanish Peaks dike swarm, Colorado, and Shiprock dike, New Mexico, J. Geophys. Res. 74, 1505–1514, 1969.

23 R.S. Cockerham and J.M. Hall, Magnetic properties and paleomagnetism of some DSDP Leg 33 basalts and sediments and their tectonic implications, J. Geophys. Res. 81, 4207–4222, 1976.

24 Johnson, H.P. and Melson, W.G., Electron microprobe analyses some titanomagnetite grains from Hole 395A, Deep Sea Drilling Project Leg 45, in: W.G. Melson, P. Rabinowitz et al., Initial Reports of Deep Sea Drilling Project 45, 575–579, 1979.

25 R. Freer, Diffusion in silicate minerals and glasses: a data digest and guide to the literature, Contrib. Mineral. Petrol. 76, 440–454, 1981.

26 O. Oshima, Mineralogical aspects of volcanic eruption, Bull. Volcanol. Soc. Jpn. 20, 275–298, 1975.

27 M.L. Wayman and M.E. Evans, Oxide microstructures and the magnetic properties of Leg 37 basalts, Can. J. Earth Sci. 14, 656–663, 1977.

28 H. Kinoshita, T. Furuta and H. Kawahata, Magnetic properties of rocks in connection with the alteration from 504B, Deep Sea Drilling Project Leg 83, in: Initial Reports of Deep Sea Drilling Project 83 (in press).